

Highly variable magmatic accretion at the ultraslow-spreading Gakkel Ridge

<https://doi.org/10.1038/s41586-024-07831-0>

Received: 27 April 2023

Accepted: 15 July 2024

Published online: 21 August 2024

Open access

 Check for updates

Tao Zhang¹, Jiabiao Li^{1✉}, Xiongwei Niu¹, Weiwei Ding¹, Yinxia Fang¹, Jian Lin^{2,3}, Yejian Wang¹, Caicai Zha³, Pingchuan Tan¹, Fansheng Kong¹, Jie Chen⁴, Xiaodong Wei¹, Jianggu Lu¹, Jérôme Dymant⁴ & Jason P. Morgan²

Crustal accretion at mid-ocean ridges governs the creation and evolution of the oceanic lithosphere. Generally accepted models^{1–4} of passive mantle upwelling and melting predict notably decreased crustal thickness at a spreading rate of less than 20 mm year⁻¹. We conducted the first, to our knowledge, high-resolution ocean-bottom seismometer (OBS) experiment at the Gakkel Ridge in the Arctic Ocean and imaged the crustal structure of the slowest-spreading ridge on the Earth. Unexpectedly, we find that crustal thickness ranges between 3.3 km and 8.9 km along the ridge axis and it increased from about 4.5 km to about 7.5 km over the past 5 Myr in an across-axis profile. The highly variable crustal thickness and relatively large average value does not align with the prediction of passive mantle upwelling models. Instead, it can be explained by a model of buoyant active mantle flow driven by thermal and compositional density changes owing to melt extraction. The influence of active versus passive upwelling is predicted to increase with decreasing spreading rate. The process of active mantle upwelling is anticipated to be primarily influenced by mantle temperature and composition. This implies that the observed variability in crustal accretion, which includes notably varied crustal thickness, is probably an inherent characteristic of ultraslow-spreading ridges.

The mid-ocean ridge is an important window into Earth's interior processes. It is commonly viewed that the mantle beneath mid-ocean ridges upwells passively owing to viscous drag from the diverging tectonic plates, causing pressure-release melting^{1,2}. Passive mantle upwelling models explain well the observed relatively uniform crustal thickness at fast-spreading ridges. At ultraslow-spreading ridges (full spreading rate <20 mm year⁻¹)⁴, the crustal thickness should decline substantially because the thick lithosphere inhibits either melting or melt migration^{5,6}. This perspective has been challenged by the recent geophysical observations of substantial time-varying and sometimes thick local crust (up to 10 km) at ultraslow-spreading ridges^{7–12}. Various 'anomalous' local factors, including mantle temperature, mantle composition, mantle plumes and focused melt supply, have been proposed to explain the varied melt supply^{10,11,13–16}. Nevertheless, the fundamental dynamics governing crustal accretion at ultraslow-spreading ridges remain elusive.

The slower spreading (full spreading rate of about 10 mm year⁻¹) eastern Gakkel Ridge in the Arctic Ocean is an ideal location to investigate melting processes because here crustal accretion is not directly affected by oblique spreading, large-offset transform faults or nearby hotspots (Fig. 1a,b and Extended Data Fig. 1). We conducted a geophysical survey along the eastern Gakkel Ridge between 76° and 100° E using the icebreaker 'Xuelong 2', during the Joint Arctic Scientific Mid-ocean ridge Insight Expedition (JASMIInE). A high-resolution seismic survey

was conducted using an OBS array, which was previously thought to be immensely challenging owing to the severe sea-ice conditions (Supplementary Fig. 1).

Evidence for highly variable crust

Most geological and geophysical surveys along the 1,800-km-long Gakkel Ridge have been conducted to the west of 85° E. The JASMIInE study region, located in the eastern Gakkel Ridge, is divided into three distinct topographic segments centred at 85° E, 92° E and 100° E, respectively (Fig. 1a and Extended Data Fig. 1). Overall, the mean crustal thickness (excluding sediments) determined by seismic tomography and gravity modelling is 5.5 km along the 240-km-long axial profile. The segment-averaged crustal thicknesses of the three segments from west to east are 5.2 km, 5.6 km and 6.2 km, respectively (Fig. 1c,d). The maximum crustal thickness reaches 7.5 km at 85° E. Constrained partly by seismic data, the best-fitting gravity model suggests maximum values of crustal thickness of 8.0 km and 8.9 km at centres of the 92° E and 100° E segments, respectively (Extended Data Fig. 5). Within these three segments, the crustal thicknesses at the centres exceed twice those at their segment ends. The thickness of the upper crust (defined by $V_p < 6.4 \text{ km s}^{-1}$) ranges from 2 km to 5 km near volcanic centres, whereas it remains relatively uniform, approximately 3–4 km, at segment ends. The thickness of the lower crust (that is, the region

¹Key Laboratory of Submarine Geosciences, Second Institute of Oceanography, Ministry of Natural Resources, Hangzhou, China. ²Advanced Institute for Ocean Research, Department of Ocean Science and Engineering, Southern University of Science and Technology, Shenzhen, China. ³Key Laboratory of Ocean and Marginal Sea Geology, South China Sea Institute of Oceanology, Chinese Academy of Sciences, Guangzhou, China. ⁴Institut de Physique du Globe de Paris, Université Paris Cité, CNRS, Paris, France. ✉e-mail: jbli@sio.org.cn

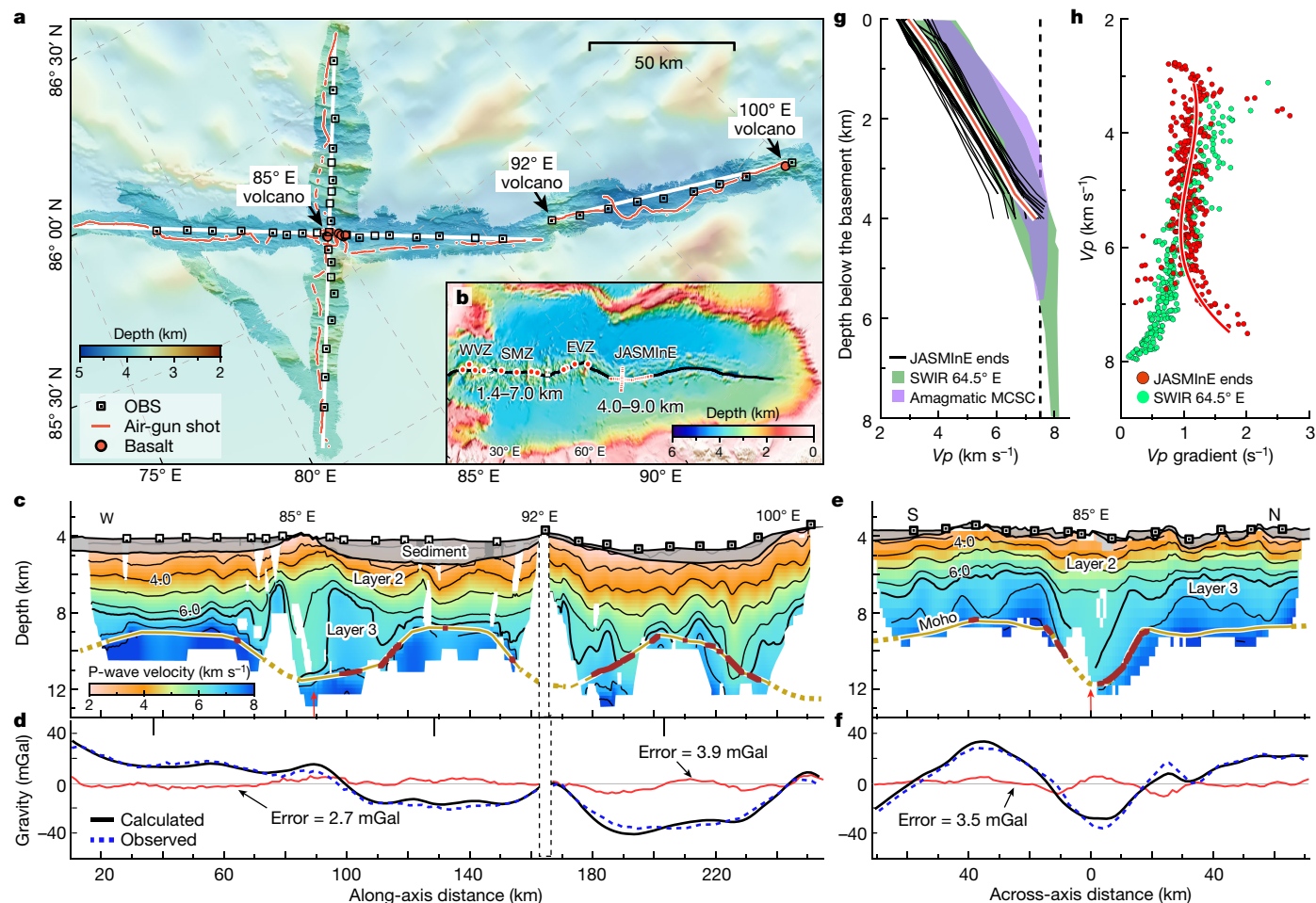


Fig. 1 | Survey layout and crustal structure of the JASMinE zone.

a, Bathymetric map of the JASMinE zone. There are three evenly spaced (about 80 km) volcanic centres at 85° E, 92° E and 100° E. **b**, Bathymetric map of the Gakkel Ridge. Locations and crustal thickness measurements of ice-station seismometers (red circles)^{16,45}, as well as the locations of OBSs (red squares) in the JASMinE zone. EVZ, Eastern Volcanic Zone; SMZ, Sparsely Magmatic Zone; WVZ, Western Volcanic Zone. **c**, Along-ridge profile illustrating the P-wave velocity (V_p) structure and the Moho from the tomographic model. The two sections comprising the profile were analysed separately, marked here by the dashed frame. Iso-velocity contours are shown every 1 km s⁻¹; the thick line marks the 6.4 km s⁻¹ contour to show the base of layer 2. Brown dots mark the position of the Moho defined by PmP arrivals. The red arrow marks where the along-axis profile intersects the across-axis profile. See Methods, Extended

Data Figs. 2–4 and Supplementary Fig. 2 for seismic data processing, model resolution and uncertainties. In the regions in which seismic rays are absent, the Moho (dashed lines) is constrained by forward modelling of gravity data (**d** and Extended Data Fig. 5). **d**, Observed and predicted free-air gravity anomaly of along-axis sections. **e**, Across-ridge profile showing tomographic V_p structure. **f**, Observed and predicted free-air gravity anomaly of the across-axis profile. **g**, 1D velocity–depth profiles of the volcanic ends in the along-axis seismic profile overlapped on those of the amagmatic SWIR 64.5° E (ref. 7) and MCSC⁸. The red line indicates the average of 1D velocity–depth profiles in volcanic ends. **h**, 1D V_p gradient– V_p profiles of volcanic ends. The profiles are extracted every 2 km at 30–60 km, 120–150 km and 190–220 km of the along-axis profile.

between $V_p = 6.4$ km s⁻¹ and the Moho) varies notably from about 4 km beneath volcanic centres to near zero close to the distal ends (Fig. 1c).

The depth gradients of V_p at the segment ends are almost constant for $V_p < 6.4$ km s⁻¹ (Fig. 1g,h). These gradients are typically associated with thin, highly fractured and altered basaltic crust^{17,18}. In some 1D profiles, the depth gradients of V_p increase abruptly from $V_p = 6.4$ km s⁻¹ to the seismic Moho, which differs notably from that seen at amagmatic zones of the ultraslow-spreading Southwest Indian Ridge (SWIR) at 64.5° E (ref. 7) and the Mid-Cayman Spreading Centre (MCSC)⁸. However, the velocity model does not allow discriminating the presence of serpentinites in the crust of segment ends. Beneath the seismic Moho of the segment end between 85° E and 92° E, low densities are required to match the gravity data (Extended Data Fig. 5). These low densities could be attributed to the serpentinitized mantle^{17,18} and/or the mantle with trapped melts¹⁹. The seismically determined crustal thickness thus provides a first-order constraint on the amount of melt at the segment ends in the JASMinE zone.

The seismically determined crustal thickness of the along-axis profile is comparable with the global average value of approximately 6 km (refs. 20,21), which is substantially higher than the predictions of about 2 km based on models of passive mantle upwelling and melting¹ and the average value of 2.7 km measured by an ice-station-based seismic experiment in the western Gakkel Ridge¹⁶. The crust at the centre of the 100° E segment is comparable in thickness with that of the magmatically robust areas on slow-spreading Mid-Atlantic Ridge (MAR) (OH-1 segment)^{22,23} and ultraslow-spreading SWIR (50.5° E)^{10,11,24} (Extended Data Fig. 6). These results, together with existing ice-station seismic observations¹⁶, reveal a highly variable crustal structure along the Gakkel Ridge, with a segment-averaged crustal thickness ranging from 1.9 km to 6.2 km and local values ranging from 1.4 km to 8.9 km (Figs. 1b and 2a).

The crust imaged across the ridge axis at the 85° E volcanic centre is generally symmetrical on conjugate flanks but exhibits substantial variations (Fig. 1e,f). The crustal thickness decreases from 7.5 km to approximately 4.5 km from the ridge axis to both flanks over a distance

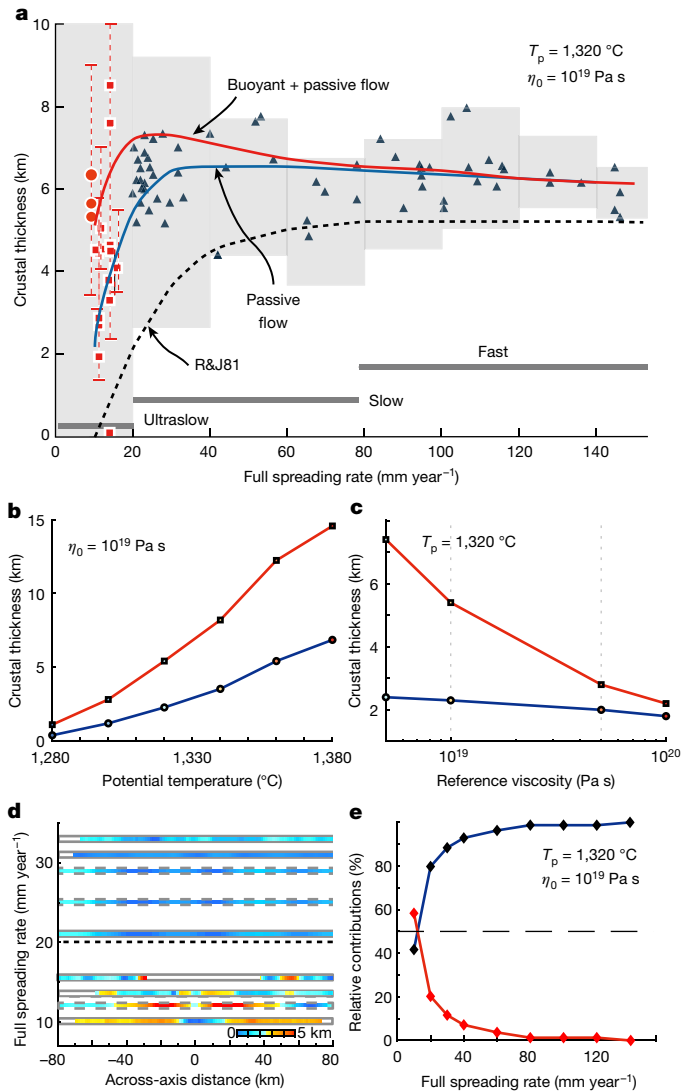


Fig. 2 | Observed crustal thickness and predictions of buoyant and passive mantle upwelling models. **a**, Segment-averaged seismic crustal thickness and modelling results versus spreading rate. Red circles mark the three segments in the JASMinE zone. Squares represent other seismic measurements at ultraslow-spreading ridges^{10,12,16,45}. Vertical dashed lines show the range of crustal thickness with local maximum and minimum values. Triangles indicate the segment-averaged crustal thickness of faster-spreading ridges⁴⁶, omitting measurements proximate to hotspots or fracture zones, which could be substantially influenced by large perturbations in mantle temperature or composition. The shaded regions represent the maxima of the binning of the seismically determined crustal thickness^{21,46,47} (Supplementary Fig. 5). The blue and red lines indicate the simulated crustal thickness of the passive mantle upwelling with the lithospheric wedge² and active mantle upwelling models, respectively. The modelled results of the pure passive mantle upwelling model¹ are also shown as a dashed line. **b, c**, Sensitivity of crustal thickness to mantle temperature and mantle viscosities at a full spreading rate of 10 mm year⁻¹. Red and blue lines indicate the results of active and passive mantle upwelling models, respectively. **d**, Across-axis profiles of seismic (solid frame) and gravity-determined (dashed frame) crustal thickness at slow-spreading and ultraslow-spreading ridges^{7,8,48–50} (Extended Data Fig. 9 and Supplementary Fig. 6). To highlight temporal variations, the minimum value of each profile was removed. From top to bottom, the profiles are MAR 5° S, MAR 2° S, MAR 2° N, MAR 26° N, MAR 45° N, MCSC, SWIR 64.5° E, Gakkal 19° E and Gakkal 85° E. **e**, Spreading-rate dependence of active versus passive mantle upwelling. The red and blue lines indicate the ratio of the crust created by active and passive mantle upwelling, respectively.

of 20–30 km, indicating an enhanced axial melt supply from about 5 Myr ago to the present. The gravity data also align with the seismically observed pattern of increased melt supply near the ridge axis (Fig. 1f and Supplementary Fig. 3). The gravity data coverage suggests that this pattern extended to a larger area (width >20 km), rather than being limited to the isolated volcano. Near the ridge axis, the thickness between iso-velocity contours of 6.0 km s⁻¹ and 6.4 km s⁻¹ can exceed 4.0 km. This intriguing observation can be compared with similar findings at the magma-rich segments of the MAR^{22,25} and the SWIR²⁴, at which deep low-velocity zones are interpreted as indications of high temperatures and melt in this setting²².

To investigate the effect of mantle compositions on melt production, fresh basalts were collected at the volcanic centres of 85° E and 100° E (Supplementary Fig. 1), at which sediments are very thin or absent. Basalts at both segments have similar ⁸⁷Sr/⁸⁶Sr (0.702576–0.702723 and 0.702575–0.702678) and εNd (8.7–9.5 and 8.7–9.3) values (Supplementary Table 1), overlapping with estimates for average global normal mid-ocean ridge basalts (MORB)^{26,27}. The water content in the mantle source varies widely between 170 ppm and 392 ppm at the 85° E volcanic centre; this range narrows to about 217 ± 13 ppm at the 100° E volcanic centre (Extended Data Fig. 1e). Combined with the data from previous studies^{26,27}, the average mantle water content in the JASMinE zone is 245 ppm, suggesting a relatively water-enriched mantle compared with the source of Pacific MORB (<200 ppm)^{27,28}. The inferred mantle potential temperature (T_p) of the JASMinE zone ranges between 1,280 °C and 1,320 °C (Extended Data Fig. 1f), with averages of about 1,300 °C and about 1,310 °C at 85° E and 100° E, respectively (Supplementary Table 2). The inferred T_p in the JASMinE zone (average T_p = 1,305 °C) falls within the global average range of 1,322 ± 56 °C (ref. 29) and is close to the T_p of Pacific MORB (average T_p = 1,300 °C) and slightly higher than the average of roughly 1,290 °C (ranging between 1,250 °C and 1,370 °C) observed within the Sparsely Magmatic Zone (SMZ) of the Gakkal Ridge (Extended Data Fig. 1f).

Variable magmatic accretion

Our observations suggest that the crust in the JASMinE zone is relatively thick, with the maximum crustal thickness being approximately twice the minimum value in both along-axis and across-axis profiles. The highly diverse crustal thickness markedly differs from the relatively uniform crust observed at fast-spreading ridges^{20,21} and contradicts the very thin crust predicted by models of passive mantle upwelling and melting^{1,2}.

The ridge axis within the JASMinE zone seems to be undergoing a surge of enhanced melt supply at present. The observed thick (7.5–8.9 km) crust at the three segment centres and the vanishing layer 3 (generally interpreted as gabbros) near segment ends suggests that there was concentrated melt supply to segment centres at depth, followed by a shallower along-axis redistribution of magma to segment distal ends. Along an ultraslow-spreading ridge axis, the permeability barrier near the base of the lithosphere could be strong³⁰ and relatively steep³¹. This could facilitate the migration of melts in the melting column towards the centre at the lithospheric base³². By contrast, across-axis melt focusing may be less efficient, as suggested by ref. 33. The virtually absent layer 3 near segment ends could be analogous to observations at other slow-spreading and ultraslow-spreading ridges^{12,22,34}, being consistent with a model in which the upper crust away from a segment centre is mostly constructed by dyke intrusions from the segment centre^{12,32,35}.

Considering the typical MORB mantle source (Supplementary Table 1), the mantle temperature and the relative water enrichment in the JASMinE zone, models of passive mantle upwelling and wet melting³⁶ predict a crustal thickness to be approximately 2 km (Supplementary Fig. 4). Focused melting along a ridge axis may redistribute melts in a segment and produces a locally thick crust at the segment centre, yet it cannot

alter the segment-averaged melt volume. A conceptual model involving melt that pools at the base of thick lithosphere until a large-volume eruption was proposed to explain the presence of episodic enhanced magmatism across the eastern SWIR and the western Gakkel Ridge^{37,38}. This model seems to be inconsistent with the observation of crust >4 km along the entire across-axis profile at the 85° E segment. Therefore, the unexpectedly thick crust observed at 85° E and 100° E cannot be straightforwardly ascribed to passive upwelling of anomalous mantle temperature or composition coupled with along-axis melt migration.

We investigated whether active mantle upwelling can explain the observed anomalously thick and time-varying crust seen at the Gakkel Ridge (Fig. 2a and Extended Data Figs. 7 and 8). We used 2D numerical models to simulate the dynamic processes of mantle upwelling and melting (Methods). Here buoyancy-driven active upwelling would be excited by lateral density gradients from thermal expansion, melt retention and melting-related mantle depletion^{39,40}. The change in the chemical composition of the mantle is because of melt extraction, which leads to a lower Fe/Mg in the residual mantle and its associated density reduction. The resulting crustal thickness reflects the combined effects of mantle buoyancy and plate separation.

For a ridge with a full spreading rate of 10 mm year⁻¹ and a global average T_p of 1,320 °C, the velocity of the passive mantle upwelling model including the lithospheric wedge² is predicted to be 7.5 mm year⁻¹ beneath the axial melting zone, with a maximum melt fraction of 8.5% and associated constant crustal thickness of about 2.1 km (Fig. 2a and Extended Data Fig. 7). By contrast, mantle upwelling in buoyant models is further accelerated, inducing an average upwelling velocity beneath the melting zone of about 15 mm year⁻¹. The associated maximum melt fraction is up to 12% (Extended Data Fig. 7), which could generate crust with an average thickness of roughly 5.2 km (Fig. 2a). Thus, given a relative normal mantle temperature and mantle compositions, the active mantle upwelling model prediction could explain the average crustal thickness along the ridge axis in the JASMinE zone.

The melt volume in the active mantle upwelling model is much more sensitive to variations in mantle temperature and viscosity than that of a passive upwelling model (Fig. 2b,c). Owing to the coupled mantle rheology and melting, changes in mantle temperature or composition give rise to positive feedback between the melt fraction and mantle upwelling velocity in the active upwelling model. In the case of a mantle rich in volatiles (for example, water and carbon dioxide) and/or fusible components, this would lead to a higher extent of melting, reducing mantle density and viscosity. Consequently, buoyant mantle upwelling would accelerate, leading to an even greater extent of melting. The variation in the predicted crustal thickness in the active upwelling model is approximately twice that of the passive model for a T_p perturbation of 100 °C (1,280–1,380 °C) with a reference mantle viscosity of 10¹⁹ Pa s (Fig. 2b and Extended Data Fig. 8a–d). Given a loosely constrained yet reasonable range of mantle viscosity (5 × 10¹⁸–10²⁰ Pa s at a depth of 100 km)⁴¹, the variation in predicted crust thickness in the active model is approximately ten times that of the passive upwelling model (Fig. 2c and Extended Data Fig. 8e–h).

The high sensitivity of active mantle upwelling amplifies the effects of mantle heterogeneity on melt production. Further considering that the melting zone is small beneath an ultraslow-spreading ridge, the extent of melting would then be susceptible to small-scale mantle heterogeneities, which could more frequently trigger marked variations in mantle buoyancy. This susceptibility may account for the observed high-amplitude oscillations (>2 km) of crustal thickness through time at ultraslow-spreading ridges (Fig. 2d, Extended Data Fig. 9 and Supplementary Fig. 6). In the magmatic zones of ultraslow-spreading ridges, mantle domains metasomatized by slab-derived material (SWIR 50° E (ref. 13)), fertile mantle (SWIR 57–60° E (ref. 14)) and/or water-enriched mantle (JASMinE zone) may lead to increased melt production and reduced mantle viscosities. Active mantle upwelling should be more intensive in these regions, which will further enhance melting.

At amagmatic zones, in which extensive serpentinized peridotites have been collected, the subaxial mantle could be either more refractory and viscous (SWIR 0–16° E (ref. 42), 64.5° E (ref. 43) and SMZ⁴⁴) or colder (SMZ; Extended Data Fig. 1f). These effects would reduce both melt fraction and the upwelling velocity of the buoyant mantle, thereby decreasing its melt production.

Spreading-dependent active upwelling

Extending our modelling approach to the global mid-ocean ridge, we find that the importance of active mantle upwelling on melt production increases with decreasing spreading rate (Fig. 2e). At fast-spreading and intermediate-spreading ridges, a notable fraction of the relatively uniform crust is formed by a high degree of melting in a relatively large melting zone that arises from steady-state passive mantle upwelling, so that the contribution of buoyant mantle upwelling is not prominent. Here the oscillations in crustal thickness, excluding measurements near hotspots or fracture zones, are much subdued (about 2 km) for passive mantle upwelling (Fig. 2a). At slow-spreading and ultraslow-spreading ridges with relatively hot, volatile-rich or fertile mantle, active mantle upwelling could dominate over passive mantle upwelling and locally generate excess melts and thick crust. The high sensitivity of active mantle upwelling, coupled with ubiquitous local mantle temperature and compositional heterogeneity, leads us to suggest that the relatively large variations (up to 5 km) in crustal thickness are an intrinsic characteristic of ultraslow-spreading ridges (Fig. 2d). The spreading-rate dependence of the relative importance of active mantle upwelling versus passive mantle upwelling is predicted to strongly shape the variability in crustal accretion of the global mid-ocean ridges.

Online content

Any methods, additional references, Nature Portfolio reporting summaries, source data, extended data, supplementary information, acknowledgements, peer review information; details of author contributions and competing interests; and statements of data and code availability are available at <https://doi.org/10.1038/s41586-024-07831-0>.

- Reid, I. & Jackson, H. R. Oceanic spreading rate and crustal thickness. *Mar. Geophys. Res.* **5**, 165–172 (1981).
- Bown, J. W. & White, R. S. Variation with spreading rate of oceanic crustal thickness and geochemistry. *Earth Planet. Sci. Lett.* **121**, 435–449 (1994).
- Shen, Y. & Forsyth, D. W. Geochemical constraints on initial and final depths of melting beneath mid-ocean ridges. *J. Geophys. Res. Solid Earth* **100**, 2211–2237 (1995).
- Dick, H. J. B., Lin, J. & Schouten, H. An ultraslow-spreading class of ocean ridge. *Nature* **426**, 405–412 (2003).
- Cannat, M. How thick is the magmatic crust at slow spreading oceanic ridges? *J. Geophys. Res. Solid Earth* **101**, 2847–2857 (1996).
- Conley, M. M. & Dunn, R. A. Seismic shear wave structure of the uppermost mantle beneath the Mohns Ridge. *Geochem. Geophys. Geosyst.* **12**, QOAK01 (2011).
- Corbalán, A. et al. Seismic velocity structure along and across the ultraslow-spreading Southwest Indian Ridge at 64°30'E showcases flipping detachment faults. *J. Geophys. Res. Solid Earth* **126**, e2021JB022177 (2021).
- Grevemeyer, I. et al. Episodic magmatism and serpentinized mantle exhumation at an ultraslow-spreading centre. *Nat. Geosci.* **11**, 444–448 (2018).
- Momoh, E., Cannat, M., Watremez, L., Leroy, S. & Singh, S. C. Quasi-3-D seismic reflection imaging and wide-angle velocity structure of nearly amagmatic oceanic lithosphere at the ultraslow-spreading Southwest Indian Ridge. *J. Geophys. Res. Solid Earth* **122**, 9511–9533 (2017).
- Li, J. et al. Seismic observation of an extremely magmatic accretion at the ultraslow spreading Southwest Indian Ridge. *Geophys. Res. Lett.* **42**, 2656–2663 (2015).
- Niu, X. et al. Along-axis variation in crustal thickness at the ultraslow spreading Southwest Indian Ridge (50°E) from a wide-angle seismic experiment. *Geochem. Geophys. Geosyst.* **16**, 468–485 (2015).
- Minshull, T. A., Muller, M. R. & White, R. S. Crustal structure of the Southwest Indian Ridge at 66°E: seismic constraints. *Geophys. J. Int.* **166**, 135–147 (2006).
- Liu, J. et al. Water enrichment in the mid-ocean ridge by recycling of mantle wedge residue. *Earth Planet. Sci. Lett.* **584**, 117455 (2022).
- Yu, X. & Dick, H. J. B. Plate-driven micro-hotspots and the evolution of the Dragon Flag melting anomaly, Southwest Indian Ridge. *Earth Planet. Sci. Lett.* **531**, 116002 (2020).
- Michael, P. J. et al. Magmatic and amagmatic seafloor generation at the ultraslow-spreading Gakkel ridge, Arctic Ocean. *Nature* **423**, 956–961 (2003).
- Jokat, W. et al. Geophysical evidence for reduced melt production on the Arctic ultraslow Gakkel mid-ocean ridge. *Nature* **423**, 962–965 (2003).

17. Minshull, T. A. et al. Crustal structure at the Blake Spur fracture zone from expanding spread profiles. *J. Geophys. Res. Solid Earth* **96**, 9955–9984 (1991).
18. Canales, J. P., Detrick, R. S., Lin, J., Collins, J. A. & Toomey, D. R. Crustal and upper mantle seismic structure beneath the rift mountains and across a nontransform offset at the Mid-Atlantic Ridge (35°N). *J. Geophys. Res. Solid Earth* **105**, 2699–2719 (2000).
19. Dunn, R. A. in *Treatise on Geophysics (Second Edition)* (ed. Schubert, G.) 419–451 (Elsevier, 2015).
20. Chen, Y. J. Oceanic crustal thickness versus spreading rate. *Geophys. Res. Lett.* **19**, 753–756 (1992).
21. Christeson, G. L., Goff, J. A. & Reece, R. S. Synthesis of oceanic crustal structure from two-dimensional seismic profiles. *Rev. Geophys.* **57**, 504–529 (2019).
22. Dunn, R. A., Lekić, V., Detrick, R. S. & Toomey, D. R. Three-dimensional seismic structure of the Mid-Atlantic Ridge (35°N): evidence for focused melt supply and lower crustal dike injection. *J. Geophys. Res. Solid Earth* **110**, B09101 (2005).
23. Hooft, E. E., Detrick, R. S., Toomey, D. R., Collins, J. A. & Lin, J. Crustal thickness and structure along three contrasting spreading segments of the Mid-Atlantic Ridge, 33.5°–35°N. *J. Geophys. Res. Solid Earth* **105**, 8205–8226 (2000).
24. Jian, H., Singh, S. C., Chen, Y. J. & Li, J. Evidence of an axial magma chamber beneath the ultraslow-spreading Southwest Indian Ridge. *Geology* **45**, 143–146 (2017).
25. Seher, T. et al. Crustal velocity structure of the Lucky Strike segment of the Mid-Atlantic Ridge at 37°N from seismic refraction measurements. *J. Geophys. Res. Solid Earth* **115**, B03103 (2010).
26. Gale, A., Dalton, C. A., Langmuir, C. H., Su, Y. & Schilling, J. The mean composition of ocean ridge basalts. *Geochem. Geophys. Geosyst.* **14**, 489–518 (2013).
27. Yang, A. Y. et al. A subduction influence on ocean ridge basalts outside the Pacific subduction shield. *Nat. Commun.* **12**, 4757 (2021).
28. Danyushevsky, L. V., Eggins, S. M., Falloon, T. J. & Christie, D. M. H₂O abundance in depleted to moderately enriched mid-ocean ridge magmas; part I: incompatible behaviour, implications for mantle storage, and origin of regional variations. *J. Petrol.* **41**, 1329–1364 (2000).
29. Krein, S. B., Molitor, Z. J. & Grove, T. L. Reverse Petrogen: a multiphase dry reverse fractional crystallization-mantle melting thermobarometer applied to 13,589 mid-ocean ridge basalt glasses. *J. Geophys. Res. Solid Earth* **126**, e2020JB021292 (2021).
30. Hebert, L. B. & Montési, L. G. J. Generation of permeability barriers during melt extraction at mid-ocean ridges. *Geochem. Geophys. Geosyst.* **11**, Q12008 (2010).
31. Schlindwein, V. & Schmid, F. Mid-ocean-ridge seismicity reveals extreme types of ocean lithosphere. *Nature* **535**, 276–279 (2016).
32. Magde, L. S. & Sparks, D. W. Three-dimensional mantle upwelling, melt generation, and melt migration beneath segment slow spreading ridges. *J. Geophys. Res. Solid Earth* **102**, 20571–20583 (1997).
33. Wanless, V. D., Behn, M. D., Shaw, A. M. & Plank, T. Variations in melting dynamics and mantle compositions along the Eastern Volcanic Zone of the Gakkel Ridge: insights from olivine-hosted melt inclusions. *Contrib. Mineral. Petrol.* **167**, 1005 (2014).
34. Jokat, W., Kollofrath, J., Geissler, W. H. & Jensen, L. Crustal thickness and earthquake distribution south of the Logachev Seamount, Knipovich Ridge. *Geophys. Res. Lett.* **39**, L08302 (2012).
35. Fialko, Y. A. & Rubin, A. M. Thermodynamics of lateral dike propagation: implications for crustal accretion at slow spreading mid-ocean ridges. *J. Geophys. Res. Solid Earth* **103**, 2501–2514 (1998).
36. Robinson, C. J., Bickle, M. J., Minshull, T. A., White, R. S. & Nichols, A. R. L. Low degree melting under the Southwest Indian Ridge: the roles of mantle temperature, conductive cooling and wet melting. *Earth Planet. Sci. Lett.* **188**, 383–398 (2001).
37. Cannat, M., Rommevaux-Jestin, C. & Fujimoto, H. Melt supply variations to a magma-poor ultra-slow spreading ridge (Southwest Indian Ridge 61° to 69°E). *Geochem. Geophys. Geosyst.* **4**, 9104 (2003).
38. Zhou, F. & Dymant, J. Temporal and spatial variation of seafloor spreading at ultraslow spreading ridges: contribution of marine magnetics. *Earth Planet. Sci. Lett.* **602**, 117957 (2023).
39. Parmentier, E. M. & Morgan, J. P. Spreading rate dependence of three-dimensional structure in oceanic spreading centres. *Nature* **348**, 325–328 (1990).
40. Sparks, D. W. & Parmentier, E. M. The structure of three-dimensional convection beneath oceanic spreading centres. *Geophys. J. Int.* **112**, 81–91 (1993).
41. Hirth, G. & Kohlstedt, D. Rheology of the upper mantle and the mantle wedge: a view from the experimentalists. *Geophys. Monogr.* **138**, 83–106 (2003).
42. Liu, C.-Z. et al. Archean cratonic mantle recycled at a mid-ocean ridge. *Sci. Adv.* **8**, eabn6749 (2022).
43. Meyzen, C. M., Toplis, M. J., Humler, E., Ludden, J. N. & Mével, C. A discontinuity in mantle composition beneath the southwest Indian ridge. *Nature* **421**, 731–733 (2003).
44. Liu, C.-Z. et al. Ancient, highly heterogeneous mantle beneath Gakkel ridge, Arctic Ocean. *Nature* **452**, 311–316 (2008).
45. Kristoffersen, Y., Husebye, E. S., Bungum, H. & Gregersen, S. Seismic investigations of the Nansen Ridge during the FRAM I experiment. *Tectonophysics* **82**, 57–68 (1982).
46. White, R. S., Minshull, T. A., Bickle, M. J. & Robinson, C. J. Melt generation at very slow-spreading oceanic ridges: constraints from geochemical and geophysical data. *J. Petrol.* **42**, 1171–1196 (2001).
47. Harding, J. L. et al. Magmatic-tectonic conditions for hydrothermal venting on an ultraslow-spread oceanic core complex. *Geology* **45**, 839–842 (2017).
48. Dannowski, A. et al. Seismic structure of an oceanic core complex at the Mid-Atlantic Ridge, 22°19'N. *J. Geophys. Res. Solid Earth* **115**, B07106 (2010).
49. Vaddineni, V. A., Singh, S. C., Grevemeyer, I., Audhkhasi, P. & Papenberg, C. Evolution of the crustal and upper mantle seismic structure from 0–27 Ma in the equatorial Atlantic Ocean at 2° 43'S. *J. Geophys. Res. Solid Earth* **126**, e2020JB021390 (2021).
50. Wang, T., Tucholke, B. E. & Lin, J. Spatial and temporal variations in crustal production at the Mid-Atlantic Ridge, 25°N–27°30'N and 0–27 Ma. *J. Geophys. Res. Solid Earth* **120**, 2119–2142 (2015).

Publisher's note Springer Nature remains neutral with regard to jurisdictional claims in published maps and institutional affiliations.



Open Access This article is licensed under a Creative Commons Attribution-NonCommercial-NoDerivatives 4.0 International License, which permits any non-commercial use, sharing, distribution and reproduction in any medium or format, as long as you give appropriate credit to the original author(s) and the source, provide a link to the Creative Commons licence, and indicate if you modified the licensed material. You do not have permission under this licence to share adapted material derived from this article or parts of it. The images or other third party material in this article are included in the article's Creative Commons licence, unless indicated otherwise in a credit line to the material. If material is not included in the article's Creative Commons licence and your intended use is not permitted by statutory regulation or exceeds the permitted use, you will need to obtain permission directly from the copyright holder. To view a copy of this licence, visit <http://creativecommons.org/licenses/by-nc-nd/4.0/>.

© The Author(s) 2024

Data acquisition

Active-source seismic refraction experiments with OBSs were conducted during the JASMinE expedition aboard the recently launched icebreaker 'Xuelong 2' in August 2021 (ref. 51). Two seismic profiles located at Gakkel 76–92° E and 92–100° E along the ridge axis (roughly 240 km in total) and one profile across the Gakkel 85° E (about 135 km) were recorded, at which the sea ice (thickness of 1.3 m on average) covered >80% of the sea surface. The OBSs were adapted for positioning using short-baseline and/or ultrashort-baseline systems on board. In total, 43 OBSs were deployed with spacing of about 5 km near 85° E and about 10 km for the other regions, and 42 OBSs were successfully recovered. Data from 35 OBSs were used to compute the velocity structure in this study (Fig. 1). Each OBS included three-component geophones and one hydrophone. The seismic source was an air-gun array of 2 × 32.7 litres (4,000 cubic inches) operating at an average shot interval of 32 s (approximately 30–60 m shot spacing) with a pressure of 10.79 MPa. A total of 5,252 shots were recorded.

Bathymetry, gravity and sonobuoys data, as well as rock samples, were also collected during the JASMinE expedition (Extended Data Fig. 1). Bathymetry data were collected with a SeaBeam 3020 multibeam system. A total of 108 sonobuoys were deployed to measure the sediment structure. Shipborne gravity data were recorded using a Micro-g S model gravimeter. Rock samples, primarily containing basalts, were collected at six TV-grab stations at the nearly sediment-free 85° E and 100° E volcanic centres.

Seismic data processing

The OBS data processing included corrections for OBS clock drifts, relocations of OBSs and shots using direct arrivals and seismic signal processing using band-pass filtering between 4 and 20 Hz. The final straight-line approximation of the profile was calculated by performing a least-squares fit on all shots of the profile. The depth of each OBS was initially estimated from bathymetric data and then adjusted by fitting the direct water arrivals.

Seismic phase analysis and selection

Seismic phases were identified using initial-travel-time modelling. We identified the direct water wave (Pw), the refracted waves from oceanic layers 2 (P2) and 3 (P3), the Moho reflection (PmP) and the refracted wave from the upper mantle (Pn).

The Pw and P2 arrivals were recorded by all OBSs (Supplementary Table 3), except for OBS 12. Maximum offsets of the Pn phase were observed up to 40 km (Extended Data Fig. 2 and Supplementary Fig. 2), making a good overlap control for the velocity models. Travel-time uncertainties were dominated by uncertainties in phase picking and off-profile time errors (Extended Data Table 1). According to the signal-to-noise ratio and band-pass filter parameters (4–20 Hz)⁵², we estimated the picking uncertainties to be about 50, 60, 80, 100 and 120 ms for Pw, P2, P3, PmP and Pn arrivals, respectively. To account for the difference in water depth between the true and modelled shot locations, we added an uncertainty term for each pick, with calculated values ranging from 1 ms to 130 ms (Extended Data Table 1). The extra time uncertainties were calculated by

$$T_{\text{unc}} = \frac{D_{s0} - D_{s1}}{V_{\text{water}}} - \frac{D_{s0} - D_{s1}}{V_{\text{sed}}},$$

in which T_{unc} is the time uncertainty, D_{s0} is the depth of the true shot position, D_{s1} is the depth of the modelled shot position, V_{water} is the P-wave water velocity (1.5 km s⁻¹) and V_{sed} is the average sediment velocity in our final velocity model.

Seismic velocity structure modelling

The velocity model was first obtained using the 2D forward ray-tracing software RAYINVR⁵² and then refined by the joint inversion code Tomo2D⁵³ using both the refraction and reflection travel-time information.

During forward modelling, the initial model comprised three crustal layers, representing sediments, oceanic crust layer 2 and layer 3. The thickness and velocity models for the three layers were based on the typical oceanic crustal structure at the slow-spreading MAR⁵⁴, with 1D linear velocity gradients within these layers. The initial model of sediment-layer thickness was constrained by the sonobuoy data with velocities of 1.8 km s⁻¹ at its top and 3.4 km s⁻¹ at its bottom. The initial model of oceanic layer 2 had a thickness of 2 km with velocities of 3.4 km s⁻¹ at its top and 6.4 km s⁻¹ at its bottom. The initial model of oceanic layer 3 had a thickness of 4 km with velocities of 6.4 km s⁻¹ at its top and 7.0 km s⁻¹ at its base. The initial model of the upper mantle had a velocity of 8.0 km s⁻¹ beneath the Moho. Horizontal node spacing within oceanic layers 2 and 3 was 5 km and 10 km, respectively. The node spacing was 20 km in the upper mantle. The velocities and boundaries were adjusted manually by trial and error⁵².

The results of forward modelling (Extended Data Fig. 2) were used as the initial models of the inversion. The velocity model was parameterized as a sheared mesh hanging beneath the seafloor; it was then interpolated to form a continuous velocity field. The sheared mesh allowed accurate travel-time calculation by ray-bending and graph methods, whereas the velocity field was estimated on the basis of the travel-time residuals⁵³. For the across-axis profile, the horizontal correlation length increased from 1 km at the top to 4 km at the bottom, whereas the vertical correlation length increased from 1 km at the top to 6 km at the bottom. For along-axis sections, the horizontal correlation length increased from 1 km at the top to 3 km at the bottom, whereas the vertical correlation length increased from 1 km at the top to 5 km at the bottom. The correlation length of the Moho reflector was set to 2 km and 3 km for across-axis and along-axis profiles, respectively. After two iterations, the optimal P-wave models were obtained (Fig. 1c,e).

Error and uncertainty of seismic model

The root mean square misfits of the Tomo2D models along the across-axis profile and the western and eastern sections of the along-axis profile were 93, 96 and 81 ms, with corresponding χ^2 values of 1.09, 1.01 and 1.08, respectively (Extended Data Table 1). We conducted checkerboard tests to assess the resolution of the tomographic velocity models. In this study, the final velocity models were perturbed by velocity variations of ±8% in cells with varying sizes. For the across-axis model, the considered dimensions are 8 km × 10 km, 8 km × 3 km and 6 km × 2 km. Along-axis models considered dimensions of 8 km × 10 km, 8 km × 4 km and 6 km × 2 km. On the basis of these perturbed models, synthetic travel times were calculated using the same source–receiver geometry. After adding a random noise of 100 ms, the synthetic travel times were inverted for the output models, using the same starting models that we used in the inversion procedure (Extended Data Fig. 4). Checkerboard recovery is best in the sediments and upper crust; at greater depths, the resolution is better in the vertical direction than in the horizontal direction. Resolution is poor at edges of models, at which the ray coverage is limited. The models have relatively good recoveries for the 8 km × 4 km anomaly and 8 km × 3 km anomaly along-axis and across-axis profiles, respectively. We also computed the derivative weight sum, which was the column-sum vector of the Fréchet velocity kernel and served as a measure of the linear sensitivity of the inversion. The derivative weight sum shows better coverage in the upper crust than in the lower crust (Extended Data Fig. 3a,b).

To assess the uncertainties and robustness of the final velocity models, we used a Monte Carlo method⁵³. We generated 100 1D initial

velocity models with randomly perturbed velocities for each profile. The velocity perturbations for all of the layers in the starting models ranged from -5% to 5% . Furthermore, we perturbed the Moho depth in along-axis sections within the range 9–12 km and in the across-axis profile within the range 8–11 km. Using the corresponding 100 reference models for both along-axis and across-axis profiles, we estimated inversion uncertainties based on the standard deviation of all solutions (Extended Data Fig. 3c–g), which is less than 0.1 km s^{-1} in the upper crust across all three models. Meanwhile, the standard deviations of velocities in the lower crust ranged from 0.1 to 0.2 km s^{-1} for both along-axis and across-axis profiles. The Moho depth uncertainties are within the range $\pm 0.1 \text{ km}$ to $\pm 0.5 \text{ km}$.

Sonobuoy data analysis

The disposable sonobuoys were equipped with a 5–2,400 Hz hydrophone, which radioed the signals back at a water depth of 60 m. In this study, we use 65 sonobuoys with relatively high data quality. Most of them have offsets ranging from 6 km to 10 km, with a maximum range of approximately 20 km.

Profiles of sonobuoy data were generated using a process similar to that of single-channel seismic surveys. For each shot, we calculated the midpoint position between the source and receiver based on their GPS coordinates. Next, we extracted the depth of this midpoint from the multibeam bathymetry data. A time shift was then applied to the data of each shot according to the travel time of seafloor reflection and midpoint depth, assuming a seawater velocity of $1,500 \text{ m s}^{-1}$. To enhance the data quality, we used a processing sequence that included low-cut filtering (2–3 Hz), high-energy noise suppression (remove three times the average amplitude) and single-trace predictive deconvolution (a filter length of 160 ms and a prediction distance of 64 ms). Finally, two-way travel time was converted to depth using regional sedimentary velocities from ref. 55. The depth of the basement was identified as a transition from high-amplitude reflections to semitransparent with low or few indistinct reflections (Supplementary Fig. 7).

Gravity data analysis

For the JASME zone, we calculated mantle Bouguer anomalies (MBA) by subtracting the gravity effects of a water layer (determined by bathymetry data), a sediment layer (constrained by sonobuoy data) and a constant crustal thickness of 5 km from the shipborne free-air gravity anomalies^{56,57}. The calculation was conducted using the 'gravfft' model of the Generic Mapping Tools software⁵⁸. The densities of the water, sediment, crust and mantle layers were assumed to be 1.03, 2.0, 2.7 and 3.3 g cm^{-3} , respectively. For the Gakkal Ridge between 6° W and 105° E , the same approach was applied to obtain the MBA. Satellite altimetric gravity data (DTU21)⁵⁹ and IBCAO 4.0 (ref. 60) were used in the calculation. Residual MBA (RMBA; Extended Data Fig. 1c) was calculated by removing the gravity effect of lithosphere thermal cooling related to seafloor age⁵⁶. The mantle thermal structure of the Gakkal Ridge was calculated using the method in ref. 61 based on a state-of-the-art global model of seafloor age⁶². This thermal structure was then converted into density variations. The gravity effects of mantle thermal variations, which are consistent with predictions from the numerical geodynamic model used in this study (Supplementary Fig. 3), were removed from the MBA data to obtain the RMBA data.

The best-fitting density model was achieved with Geosoft Oasis montaj v9.7. In the areas covered by seismic rays, the density is converted from the P-wave velocity model using velocity contours and matching velocity–density relationships for the oceanic crust⁶³ and serpentinized mantle⁶⁴ (Extended Data Fig. 5). In the areas without seismic rays, the density refers to the densities of neighbouring areas and areas with similar topography. In the areas with seismic rays, we use the Moho from the tomographic model, whereas in the areas without seismic rays, we adjust the level of Moho to achieve a good fit to the observation.

Rock samples analysis

Fresh quenched glass chips and some plagioclase-olivine-phyric basalts were carefully selected from six TV-grab stations at 85° E and 100° E volcanic centres. Sr–Nd isotopes of 14 basaltic rock powers and glass chips were measured at Nanjing FocuMS Technology Co. Ltd. using a Nu Plasma II multi-collector inductively coupled plasma mass spectrometer. The detailed digestion and Sr–Nd purification follow the procedures described in ref. 65. Raw data of isotopic ratios were internally corrected for mass fractionation by normalizing to $^{86}\text{Sr}/^{88}\text{Sr} = 0.1194$ for Sr and $^{146}\text{Nd}/^{144}\text{Nd} = 0.7219$ for Nd. International isotopic standards (NIST SRM 987 for Sr and JNdi-1 for Nd) were periodically analysed to correct instrumental drift. The analytical data are given in Supplementary Table 1. USGS reference materials of BCR-2, BHVO-2 and AVG-2 were run together with our samples and their results agreed with previous publications within analytical uncertainty⁶⁶.

Major elements and H_2O contents on 43 glasses were determined at the Key Laboratory of Submarine Geosciences, Second Institute of Oceanography, Ministry of Natural Resources. The major-element compositions were identified on a JEOL JXA-8100 electron microprobe using an accelerating voltage of 15 kV, a beam current of 20 nA and a spot size of $15 \mu\text{m}$. Natural minerals and synthetic oxides were used as standards and a program based on the ZAF procedure was used for data correction. The analytical error for most elements was less than 5%. Compositions were then determined using the average of three analyses per glass (Supplementary Table 2). The H_2O contents of the glasses were analysed by Fourier-transform infrared spectroscopy following ref. 67. Analyses are the average of five point determinations (Supplementary Table 2). Replicate analyses of each glass wafer were typically reproducible to $\pm 5\%$. The H_2O was then corrected to calculate the water contents of the mantle source using the method PRIMELT3 MEGA.XLSM⁶⁸.

Numerical modelling

We used the geodynamic code ASPECT^{69,70} to perform 2D numerical models to simulate the dynamic processes of the sub-ridge mantle upwelling and melting⁷¹. The rectangular model domains extend to a depth of 100 km and have a horizontal width range of 200–800 km, depending on the spreading rates.

The half-spreading rate (U_0) is imposed on the top surface. The left boundary, which symbolizes the ridge axis, is designed as a free slip to inhibit lateral mantle flow. The bottom and right boundaries exert no traction, permitting materials to pass through them unimpeded. The top surface is set at 0° C , whereas the temperature at the bottom boundary is calculated by adding the T_p and an adiabatic temperature gradient of about $0.3^\circ \text{ C km}^{-1}$. All remaining boundaries are heat insulating. All compositional fields at the inflow bottom boundary are set to zero. The initial temperature is uniformly distributed horizontally, determined arbitrarily by a combination of an adiabat for the given T_p and cooling from the top by an age of 50 Myr. All compositional fields are initially set to zero.

Mantle viscosity depends on temperature and pressure and is also weakened by retained melts, as follows:

$$\eta = \eta_0 \exp[(E + \rho_0 ghV)/(RT) - (E + \rho_0 gh_0V)/(RT_0)] e^{-45\phi},$$

in which η_0 is the reference mantle viscosity under the pressure at the model bottom and temperature T_0 , R is the universal gas constant, E is activation energy, V is activation volume, h_0 is the height of the model domain (that is, 100 km), T_0 is the reference mantle temperature and ϕ is the melt retention. The values of these parameters are listed in Supplementary Table 4. The minimum and maximum cutoff values of 10^{18} Pa s and 10^{23} Pa s are applied to limit mantle viscosity for numerical simulations.

In buoyant models, buoyancy arises from lateral variations in mantle temperature, mantle depletion and melt retention. The variation in density is calculated by

$$\Delta\rho = -\rho_0\alpha(T - T_0) - \rho_\zeta\zeta - \rho_\phi\phi,$$

in which ρ_0 is the reference density of the unmelted mantle at T_0 and ρ_ζ and ρ_ϕ are density reductions owing to mantle depletion and melt retention, respectively. In passive models, no buoyancy is considered.

The spreading-rate-dependent crustal production, for both cases of passive and buoyant upwelling, is tested by performing numerical models with varying half spreading rates ($U_0 = 5\text{--}70\text{ mm year}^{-1}$) for a given T_p of $1,320\text{ }^\circ\text{C}$. To focus on the crustal production at the Gakkel Ridge ($U_0 = 5\text{ mm year}^{-1}$), we also perform models with varying potential mantle temperature and reference mantle viscosity. The reference mantle viscosity ($\eta_0 = 5 \times 10^{18}\text{--}10^{20}\text{ Pa s}$) is from ref. 41 and is strongly dependent on mantle temperature, pressure and mantle water content. To justify the uniform 6.0 km crust at fast spreading rates, we assume that 85% of the generated melts within a particular pooling width (W_0), such as 80 km , are instantly extracted to form oceanic crust. The steady-state crustal thickness is calculated following ref. 72.

Data availability

All geophysical data, including bathymetry data, seismic data and picks of phases and gravity data, that support the findings of this study are available at Figshare (<https://doi.org/10.6084/m9.figshare.25557210>; ref. 73). All geochemistry data are available at Figshare (<https://doi.org/10.6084/m9.figshare.26123878>; ref. 74). Source data are provided with this paper.

Code availability

Seismic data processing and analysis were performed using the Seismic Unix software v41 on operating system openSUSE 11.2. Travel-time picking and modelling were performed using the RAYINVR software⁵². The inversion models were performed using the Tomo2D software⁵³. The mantle Bouguer anomaly was calculated with Generic Mapping Tools software v6.4. The best-fitting density model was achieved with Geosoft Oasis montaj v9.7. Numerical simulations were performed using the open-source geodynamic code ASPECT v2.0.1 (refs. 69,70). The numerical codes and results are available for download at Figshare (<https://doi.org/10.6084/m9.figshare.25557210>; ref. 73).

51. Ding, W. et al. Submarine wide-angle seismic experiments in the High Arctic: the JASMIN Expedition in the slowest spreading Gakkel Ridge. *Geosyst. Geoenviron.* **1**, 100076 (2022).
52. Zelt, C. A. & Smith, R. B. Seismic traveltimes inversion for 2-D crustal velocity structure. *Geophys. J. Int.* **108**, 16–34 (1992).
53. Korenaga, J. et al. Crustal structure of the southeast Greenland margin from joint refraction and reflection seismic tomography. *J. Geophys. Res. Solid Earth* **105**, 21591–21614 (2000).
54. White, R. S., McKenzie, D. & O’Nions, R. K. Oceanic crustal thickness from seismic measurements and rare earth element inversions. *J. Geophys. Res. Solid Earth* **97**, 19683–19715 (1992).
55. Nikishin, A. M., Gaina, C., Petrov, E. I., Malyshev, N. A. & Freiman, S. I. Eurasia Basin and Gakkel Ridge, Arctic Ocean: crustal asymmetry, ultra-slow spreading and continental rifting revealed by new seismic data. *Tectonophysics* **746**, 64–82 (2018).

56. Kuo, B.-Y. & Forsyth, D. W. Gravity anomalies of the ridge-transform system in the South Atlantic between 31 and 34.5° S : upwelling centers and variations in crustal thickness. *Mar. Geophys. Res.* **10**, 205–232 (1988).
57. Lin, J., Purdy, G. M., Schouten, H., Sempere, J.-C. & Zervas, C. Evidence from gravity data for focused magmatic accretion along the Mid-Atlantic Ridge. *Nature* **344**, 627–632 (1990).
58. Wessel, P. et al. The generic mapping tools version 6. *Geochem. Geophys. Geosyst.* **20**, 5556–5564 (2019).
59. Andersen, O. B., Knudsen, P., Kenyon, S., Holmes, S. & Factor, J. K. in *International Association of Geodesy Symposia* Vol. 149 (eds Freymueller, J. T. & Sánchez, L.) 77–81 (Springer, 2019).
60. Jakobsson, M. et al. The international bathymetric chart of the Arctic Ocean version 4.0. *Sci. Data* **7**, 176 (2020).
61. Behn, M. D., Boettcher, M. S. & Hirth, G. Thermal structure of oceanic transform faults. *Geology* **35**, 307–310 (2007).
62. Seton, M. et al. A global data set of present-day oceanic crustal age and seafloor spreading parameters. *Geochem. Geophys. Geosyst.* **21**, e2020GC009214 (2020).
63. Carlson, R. L. & Herrick, C. N. Densities and porosities in the oceanic crust and their variations with depth and age. *J. Geophys. Res. Solid Earth* **95**, 9153–9170 (1990).
64. Christensen, N. I. Serpentinities, peridotites, and seismology. *Int. Geol. Rev.* **46**, 795–816 (2004).
65. Ma, X., Meert, J. G., Xu, Z. & Yi, Z. Late Triassic intra-oceanic arc system within Neotethys: evidence from cumulate appinite in the Gangdese belt, southern Tibet. *Lithosphere* **10**, 545–565 (2018).
66. Weis, D. et al. High-precision isotopic characterization of USGS reference materials by TIMS and MC-ICP-MS. *Geochem. Geophys. Geosyst.* **7**, Q08006 (2006).
67. Zong, T. et al. H_2O in basaltic glasses from the slow-spreading Carlsberg Ridge: implications for mantle source and magmatic processes. *Lithos* **332–333**, 274–286 (2019).
68. Herzberg, C. & Asimow, P. D. PRIMELT3 MEGA.XLSM software for primary magma calculation: peridotite primary magma MgO contents from the liquidus to the solidus. *Geochem. Geophys. Geosyst.* **16**, 563–578 (2015).
69. Heister, T., Dannberg, J., Gassmüller, R. & Bangerth, W. High accuracy mantle convection simulation through modern numerical methods – II: realistic models and problems. *Geophys. J. Int.* **210**, 833–851 (2017).
70. Kronbichler, M., Heister, T. & Bangerth, W. High accuracy mantle convection simulation through modern numerical methods. *Geophys. J. Int.* **191**, 12–29 (2012).
71. Zha, C., Zhang, F., Lin, J., Zhang, T. & Tian, J. On the relative importance of buoyancy and thickening of aging lithosphere in mantle upwelling and crustal production beneath global mid-ocean ridge system. *J. Geophys. Res. Solid Earth* **129**, e2023JB028432 (2024).
72. Forsyth, D. W. Crustal thickness and the average depth and degree of melting in fractional melting models of passive flow beneath mid-ocean ridges. *J. Geophys. Res. Solid Earth* **98**, 16073–16079 (1993).
73. Zhang, T. Data and Codes of JASMINe_2021. Figshare <https://doi.org/10.6084/m9.figshare.25557210> (2024).
74. Zhang, T. JASMINe2021_GeochemistryData. Figshare <https://doi.org/10.6084/m9.figshare.26123878> (2024).

Acknowledgements We are very grateful to the captain and crew of the icebreaker ‘Xuelong 2’ for a successful cruise and to Y. J. Chen, Q. Sun, Z. Shen, Z. Yu, J. Zhang and M. Cannat for helpful conversations. We thank the National Arctic and Antarctic Data Center of China. Funding was generously provided by the National Natural Science Foundation of China (42330308, 42176086), the Chinese Arctic and Antarctic Administration (CHINARE N12), Donghai Laboratory (DH-2022ZY0007) and Zhejiang Provincial Natural Science Foundation of China (LDQ23D060001).

Author contributions Conceptualization T.Z., J.Li. Methodology: T.Z., X.N., C.Z., J.C., X.W., J.Lu. Fieldwork: T.Z., J.Li, X.N., W.D., Y.F., Y.W., P.T., F.K. Seismic modelling: X.N., X.W. Visualization: T.Z., J.Li, X.N., C.Z., J.C., X.W. Funding acquisition: J.Li. Supervision: J.Li, W.D., J.Lin. Writing (original draft): T.Z., J.Li. Writing (review and editing): all authors contributed to the review and editing.

Competing interests The authors declare no competing interests.

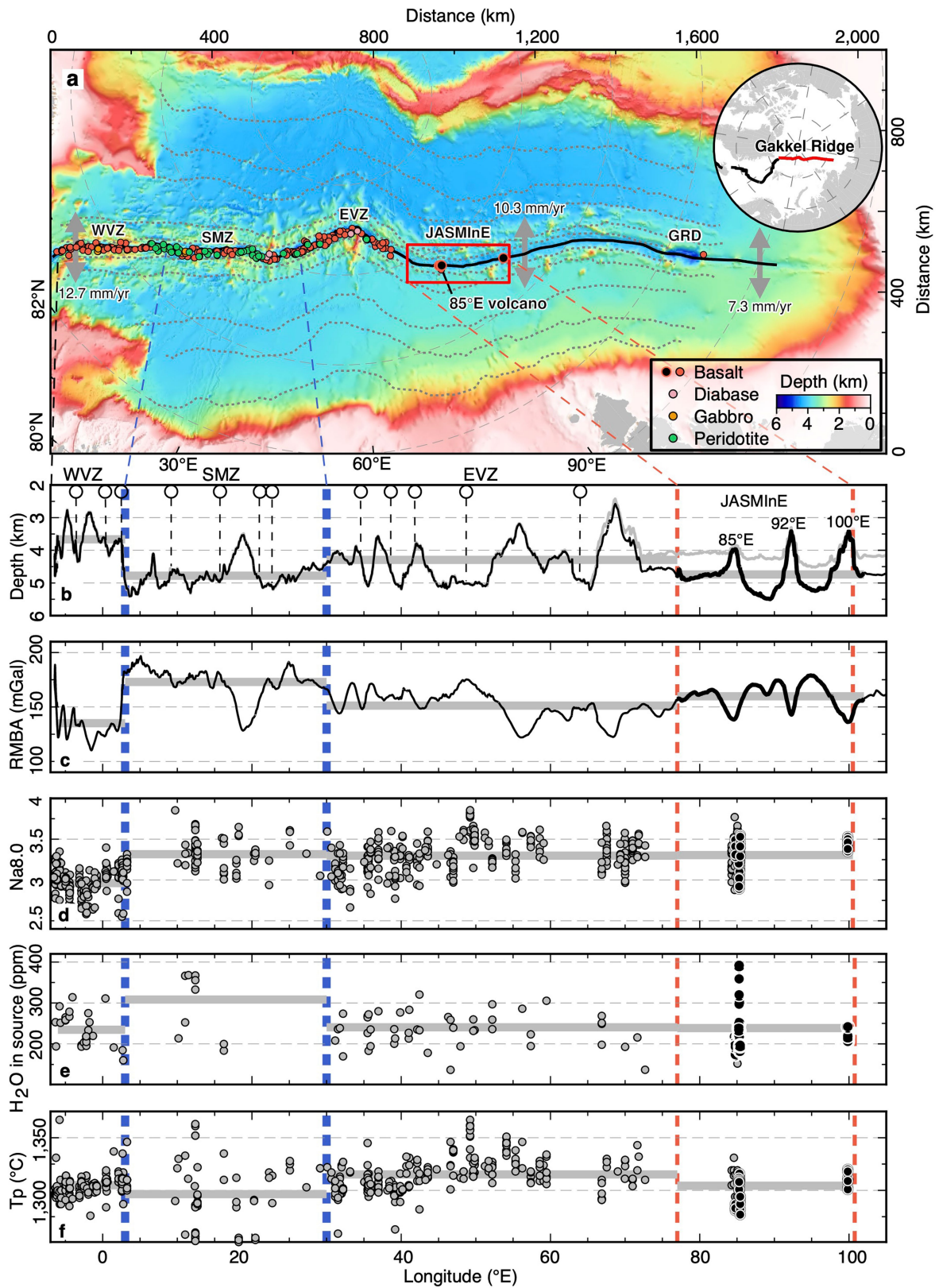
Additional information

Supplementary information The online version contains supplementary material available at <https://doi.org/10.1038/s41586-024-07831-0>.

Correspondence and requests for materials should be addressed to Jiabiao Li.

Peer review information *Nature* thanks Tim Minshull and the other, anonymous, reviewer(s) for their contribution to the peer review of this work.

Reprints and permissions information is available at <http://www.nature.com/reprints>.

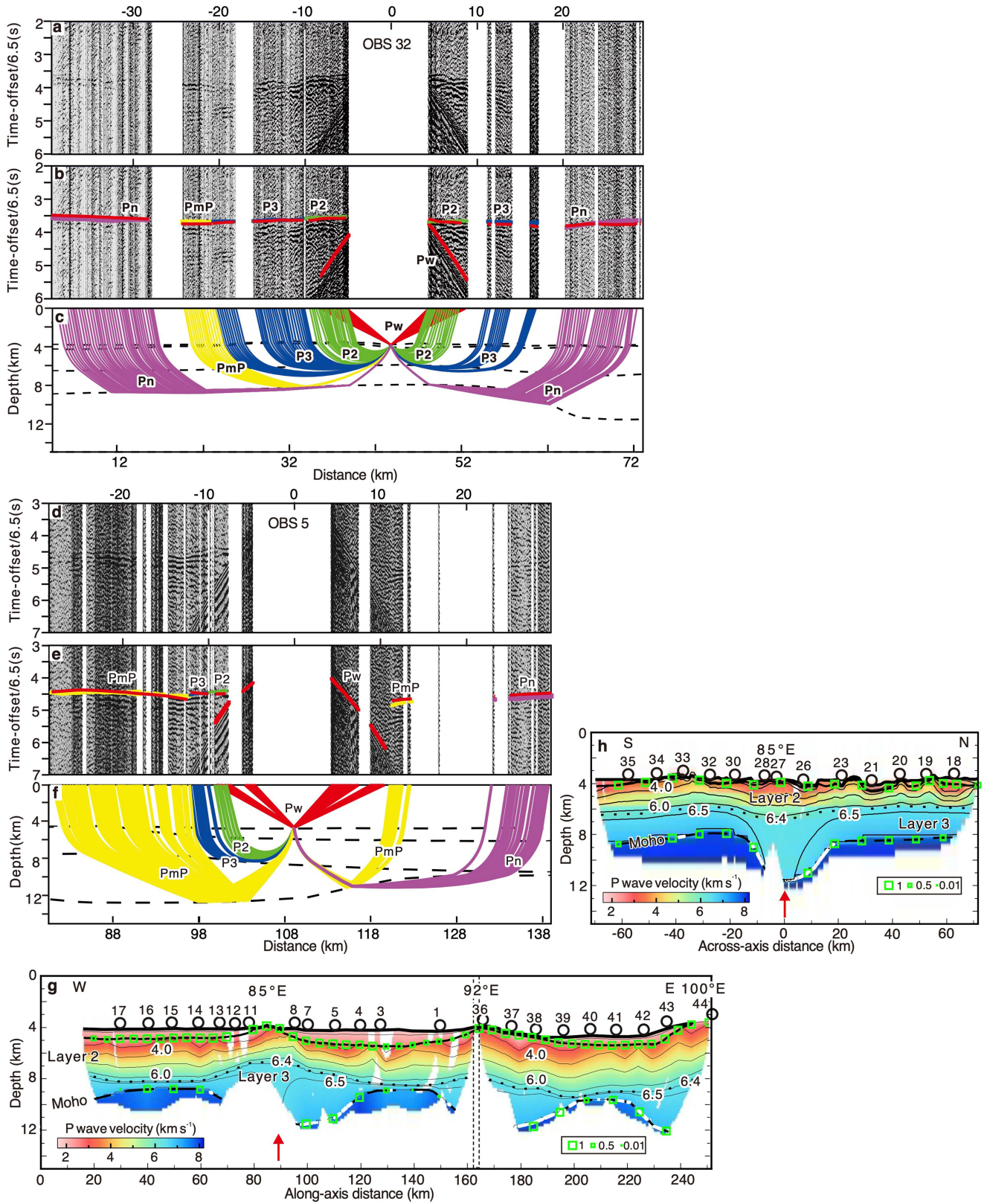


Extended Data Fig. 1 | See next page for caption.

Article

Extended Data Fig. 1 | Bathymetric map and along-axis profiles of the Gakkel Ridge. **a**, Bathymetric map of the Gakkel Ridge. The full spreading rate of the Gakkel Ridge ranges from $12.7 \text{ mm year}^{-1}$ near the Fram Strait to 7.3 mm year^{-1} close to the Laptev Sea margin. On the basis of the predominant types of rock sample obtained, the western Gakkel Ridge was divided into the Western Volcanic Zone (WVZ, basalts), the Sparsely Magmatic Zone (SMZ, peridotites) and the Eastern Volcanic Zone (EVZ, basalts)¹⁵. GRD, Gakkel Ridge Deep. **b**, Along-axis depth profiles of the seafloor (grey line) and the basement (black line). In the JASMinE zone, sediment thickness is constrained by sonobuoy data. West of the JASMinE zone, the sediment is assumed to be absent as extensive basalts and peridotites are directly exposed on the seafloor. Circles indicate the positions of seismometers on ice floes¹⁶. Most ice-floe seismometers were deployed

above the deep part (water depth of 3.8–4.8 km) of the rift valley (that is, segment ends), at which the estimated average crustal thickness is roughly 2.7 km (ref. 16). Near a volcanic centre in the WVZ, the estimated crust thickness is 7 km (ref. 45). Thick grey lines indicate average values of the basement depth. **c–f**, Along-axis variations in the RMBA, Na8.O composition of basaltic glasses, H₂O in the mantle source and calculated T_p (ref. 26). The average values of each region are indicated by horizontal grey bars. The RMBA is a crude indicator of crustal thickness and/or mantle thermal structure. Black dots indicate data from samples obtained in this study. Na8.O data suggest that the mantle beneath the Gakkel Ridge has a relatively low T_p and a reduced extent of partial melting¹⁵. T_p is calculated using the ReversePetrogen code²⁹. H₂O in source is calculated using the method PRIMELT3 MEGA.XLSM⁶⁸.



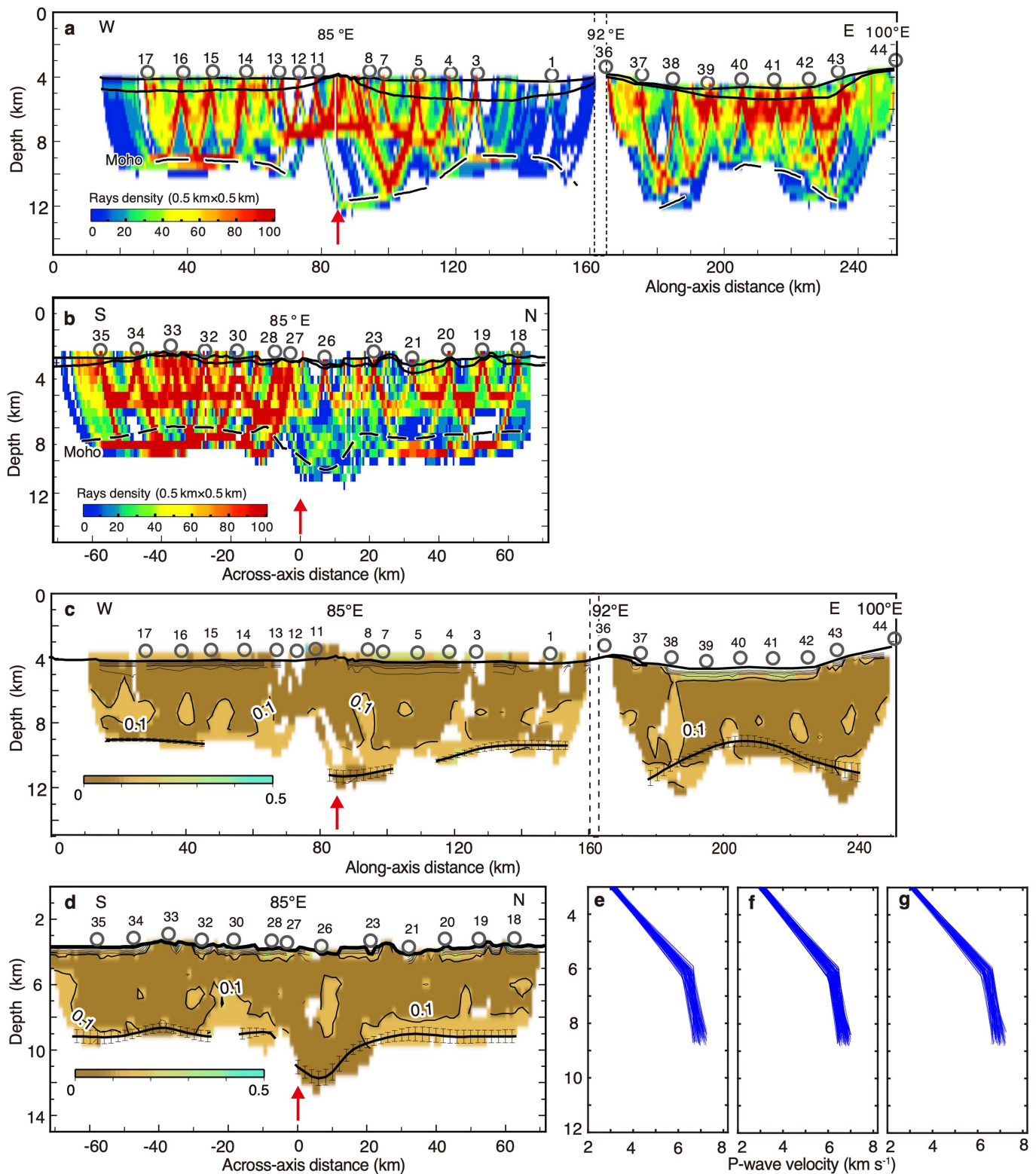
Extended Data Fig. 2 | See next page for caption.

Article

Extended Data Fig. 2 | Seismic sections and travel-time ray tracing based on the forward model of OBSs 32 and 5 and forward P-wave velocity models.

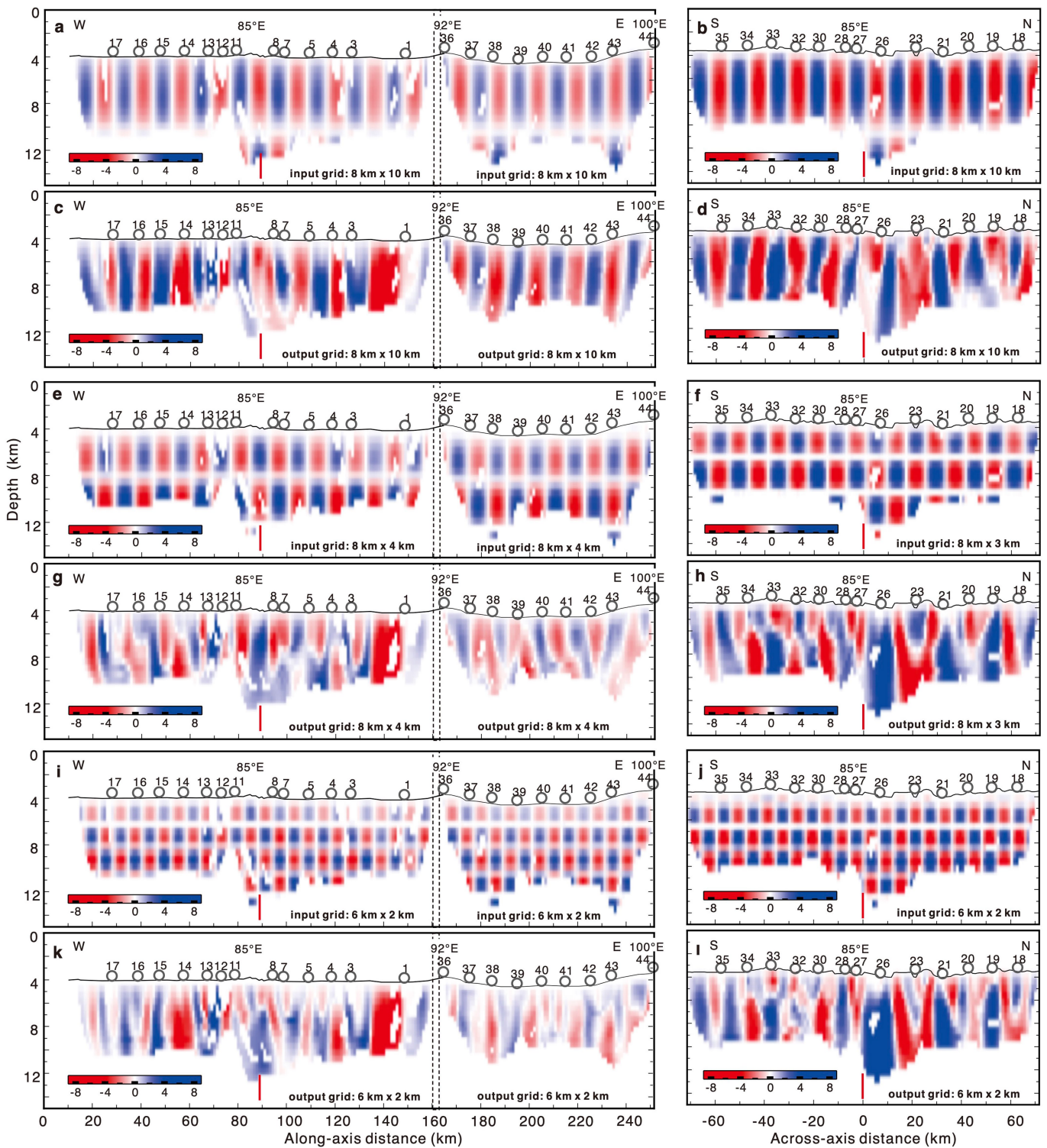
a, A seismic section of the hydrophone component of OBS 32 in the across-axis profile. **b**, The recorded section with picked and calculated travel time overlaid. Red lines represent the predicted travel time. The coloured vertical bars represent the observed travel time in the same colour of rays in panel **c**. The size of the vertical bars indicates twice the uncertainty⁵². P2 and P3, refracted rays from oceanic layers 2 and 3, respectively; PmP, reflected rays at the Moho; Pn, turning rays in the upper mantle. **c**, A simulation of ray tracing using the final forward model. The dashed black lines represent the seabed, the sediment basement, the interface between oceanic layer 2 and layer 3 and the Moho

discontinuity, from top to bottom. **d-f**, Seismic section of OBS 5. We select the two OBSs to show the good (OBS 32) and poor quality (OBS 5) of the raw OBS data. **g,h**, The forward seismic P-wave velocity structures. Thick black lines represent the seabed and sediment basement. Thin black lines indicate the contour of V_p in every 1 km s⁻¹. The dotted line represents the iso-velocity contour of 6.4 km s⁻¹. The thick dashed black lines show the Moho discontinuity, on which the sections constrained by PmP reflections are marked with thick white lines. The green rectangles along the interfaces represent the values of resolution for the velocity nodes of the top of layer 2 and the bottom of layer 3, and values greater than 0.5 are considered reliable.



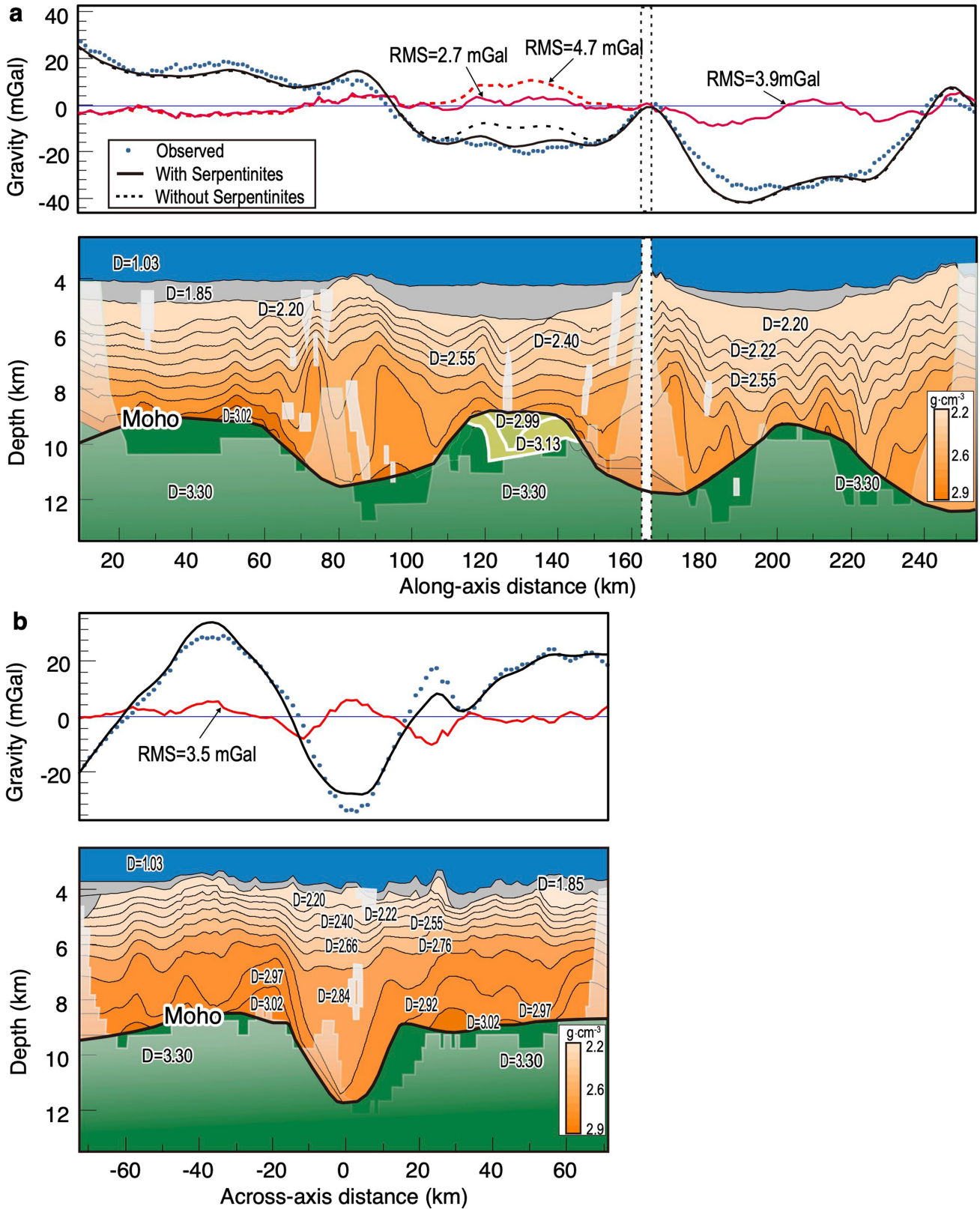
Extended Data Fig. 3 | Derivative weight sum results and uncertainties test of tomographic inversion models. **a, b.** The derivative weight sum results with horizontal and vertical grid spacings of 0.5 km. **c, d.** Standard deviation for velocity derived from ten Monte Carlo ensembles of the along-axis and across-axis crustal velocity models. The contour interval of the mean standard

deviation is 0.1 km s^{-1} . The thick contour marks the 0.1 km s^{-1} standard deviation velocity. The thick line with error bars marks the average Moho boundaries. **e-g.** The 100 1D randomly perturbed initial models for the western (**e**) and eastern (**f**) sections of the along-axis profile and the across-axis profile (**g**).



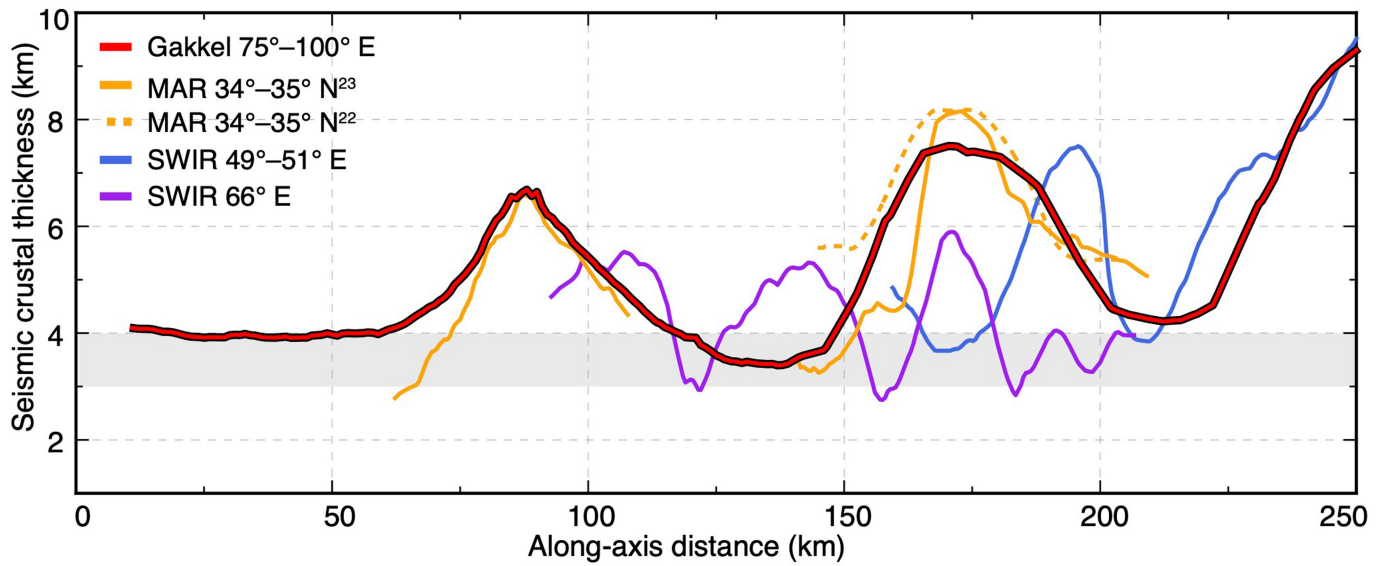
Extended Data Fig. 4 | Checkerboard resolution tests of the inversion models. The distance and depth grid spacing of the along-axis input model in panels **a**, **e** and **i** are $8\text{ km} \times 10\text{ km}$, $8\text{ km} \times 4\text{ km}$ and $6\text{ km} \times 2\text{ km}$, respectively.

For the across-axis profile, the distance and depth grid spacing in panels **b**, **f** and **j** are $8\text{ km} \times 10\text{ km}$, $8\text{ km} \times 3\text{ km}$ and $6\text{ km} \times 2\text{ km}$, respectively. Panels **c**, **d**, **g**, **h**, **k** and **l** show output models.



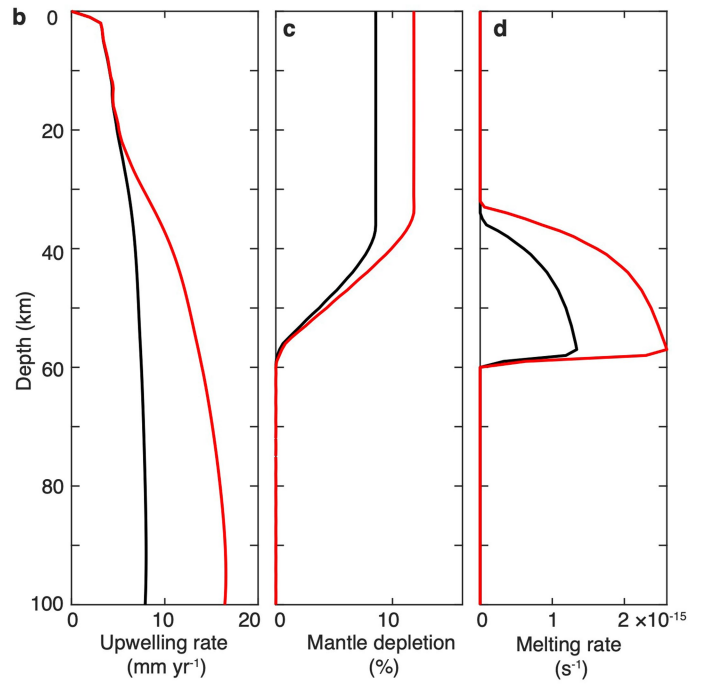
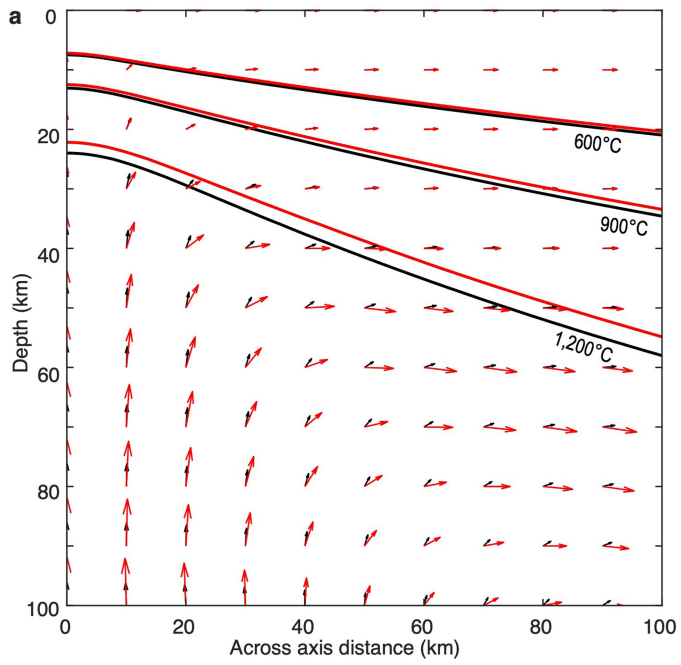
Extended Data Fig. 5 | Observed and predicted free-air gravity anomaly along and across the ridge axis. a, Along the ridge axis. **b**, Across the ridge axis. For the crustal part, we used the density structure achieved from the velocity structure, along with the velocity–density relationship for igneous crust⁶³. We also tested the presence of low densities in the mantle by applying the velocity–density relationship for serpentinitized mantle⁶⁴ and found that incorporating low-density mantle within the 120–150 km distance along the axis profile (yellow parts) led to reduced errors. These low densities may be

attributed to serpentinitized mantle^{17,18} and/or mantle with trapped melts¹⁹. A linear trend was removed from the free-air gravity anomaly of the along-axis profile. The magnitude of the linear trend is 7.5 mGal over 240 km, which may reflect the effect of the colder mantle in the east. A cooling effect was corrected from the free-air gravity anomaly of the across-axis profile (Supplementary Fig. 3). The numbers indicate density in $g \cdot cm^{-3}$. On the basis of the 138 crossovers, the root mean square is 0.2 mGal.



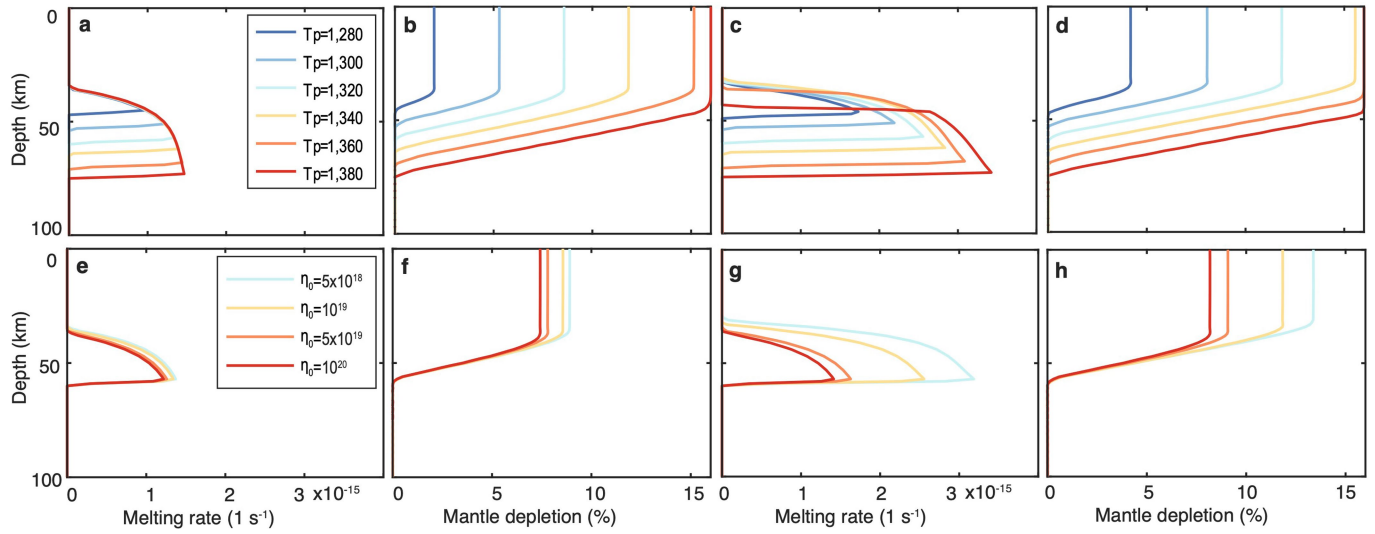
Extended Data Fig. 6 | Comparison between the along-axis crustal thickness of the JASMinE zone and other slow-spreading and ultraslow-spreading ridges. The Moho at the MAR (34–35° N)^{22,23}, the SWIR 49–51° E (ref. 10) and the SWIR 66° E (ref. 12) are defined by PmP arrivals. Although the MAR at 34–35° N

has a spreading rate roughly twice that of the JASMinE region, their crustal thicknesses and variations along the axis remain comparable^{22,23}. This pattern of anomalously thick crust at a segment centre and large along-axis variations could be observed in both slow-spreading^{22,23} and ultraslow-spreading ridges¹².



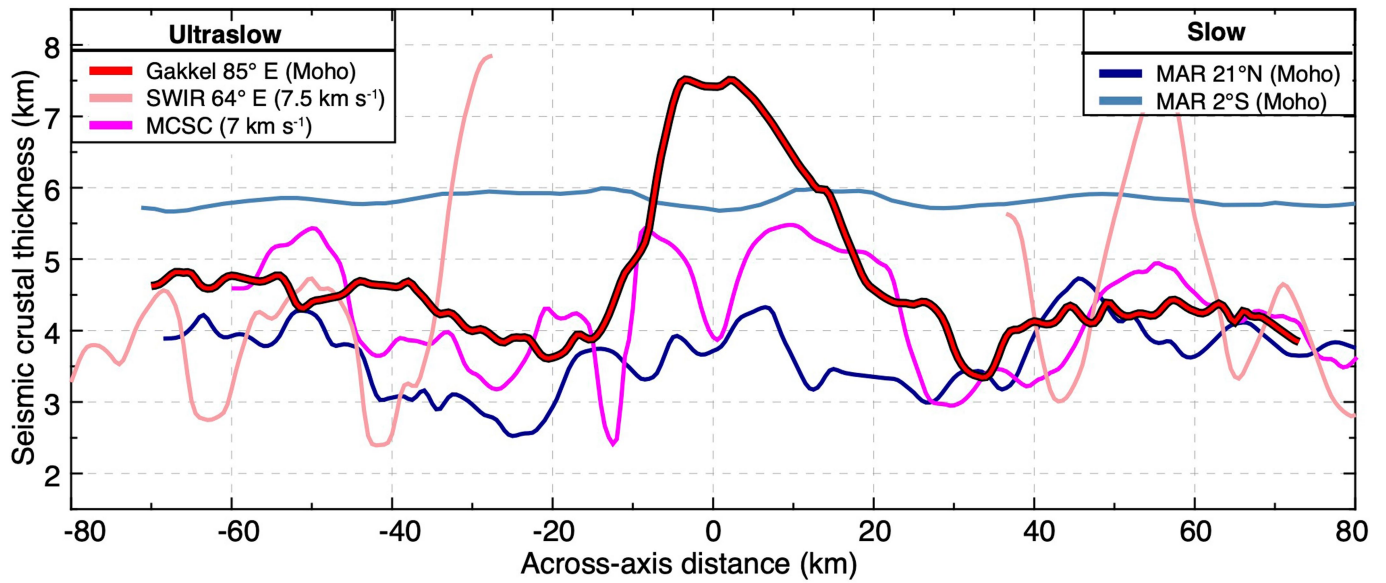
Extended Data Fig. 7 | Steady-state model results from passive (black) and buoyant (red) models with half spreading rate of 5 mm year^{-1} , T_p of $1,320 \text{ }^\circ\text{C}$ and reference mantle viscosity of 10^{19} Pa s . a, Mantle flow patterns. The solid

lines indicate the isotherms. b-d, Vertical variations of mantle upwelling rate (b), mantle depletion (c) and melting rates (d) beneath the ridge axis.



Extended Data Fig. 8 | Vertical variations of melting rate and mantle depletion. Results of the passive (a,b) and the active (c,d) mantle upwelling models at a reference mantle viscosity of 10^{19} Pa s and varying T_p . Results of the

passive (e,f) and the active (g,h) mantle upwelling models at a T_p of $1,320$ °C and varying reference mantle viscosity. All the results are calculated with a half spreading rate of 5 mm year $^{-1}$.



Extended Data Fig. 9 | Cross-axis profiles of seismically determined crustal thickness at slow-spreading and ultraslow-spreading ridges^{7,8,48,49}. For the Gakkel Ridge 85° E (this study), MAR 21° N (ref. 48) and MAR 2° S (ref. 49), the Moho is defined by PmP arrivals. The lower boundary of the crust is defined

by $v_p = 7.0 \text{ km s}^{-1}$ and $v_p = 7.5 \text{ km s}^{-1}$ for the MCSC⁸ and the SWIR 64° E (ref. 7), at which PmP arrivals are absent, respectively. Ultraslow-spreading ridges exhibit higher variations in crustal thickness than that at the slow-spreading MAR.

Article

Extended Data Table 1 | Statistics of P-wave travel-time analysis for the forward and inversion models of the JASMIInE profiles

Profile	Phases	Total picks	For-Fitted Picks	For-Fit ratio (%)	Assigned Uncertainties (ms)*	For-RMS (ms)	For χ^2	Inv-RMS (ms)	Inv- χ^2
Across-axis profile	Pw	2436	2435	99.9	50	43	0.750	/	/
	P2	1361	1236	93.4	60–133 (94)	100	1.331	/	/
	P3	2127	1821	84.1	80–210 (110)	102	0.889	/	/
	PmP	479	479	100	100–230 (128)	138	1.318	/	/
	Pn	3195	3170	99.2	120–230 (124)	122	0.969	/	/
	All		9625	9141	95.2	50–230 (98)	100	0.961	93
Western section of the along-axis profile	Pw	1531	1524	99.5	50	40	0.651	/	/
	P2	1052	886	84.2	60–154 (79)	107	1.690	/	/
	P3	1126	1001	88.9	80–188 (98)	190	3.130	/	/
	PmP	929	871	93.8	100–192 (113)	85	0.597	/	/
	Pn	1165	1114	95.6	120–155 (129)	91	0.691	/	/
	All		5802	5396	93.0	50–192 (91)	110	1.280	96
Eastern section of the along-axis profile	Pw	904	904	100	50	64	1.651	/	/
	P2	1652	1587	96.1	60–184 (115)	115	1.183	/	/
	P3	141	121	85.8	80–172 (125)	154	1.855	/	/
	PmP	883	834	94.5	101–178 (142)	96	0.434	/	/
	Pn	241	153	63.5	148–224 (182)	169	0.766	/	/
	All		3821	3599	94.2	50–224 (110)	105	1.130	81

*The values in the parentheses denote the average uncertainties of each phase.